

# THE FORMATION OF THE COLLISIONAL FAMILY AROUND THE DWARF PLANET HAUMEA

ZOË M. LEINHARDT

Department of Applied Mathematics and Theoretical Physics,  
University of Cambridge, CB3 0WA, U.K.

ROBERT A. MARCUS

Astronomy Department, Harvard University,  
60 Garden St., Cambridge, MA 02138, U.S.A.

SARAH T. STEWART

Department of Earth and Planetary Sciences, Harvard University,  
20 Oxford St., Cambridge, MA 02138, U.S.A.

*Accepted for publication in the Astrophysical Journal, March 23, 2010.*

## ABSTRACT

Haumea, a rapidly rotating elongated dwarf planet ( $\sim 1500$  km in diameter), has two satellites and is associated with a “family” of several smaller Kuiper Belt objects (KBOs) in similar orbits. All members of the Haumea system share a water ice spectral feature that is distinct from all other KBOs. The relative velocities between the Haumea family members are too small to have formed by catastrophic disruption of a large precursor body, which is the process that formed families around much smaller asteroids in the Main Belt. Here we show that all of the unusual characteristics of the Haumea system are explained by a novel type of giant collision: a graze-and-merge impact between two comparably sized bodies. The grazing encounter imparted the high angular momentum that spun off fragments from the icy crust of the elongated merged body. The fragments became satellites and family members. Giant collision outcomes are extremely sensitive to the impact parameters. Compared to the Main Belt, the largest bodies in the Kuiper Belt are more massive and experience slower velocity collisions; hence, outcomes of giant collisions are dramatically different between the inner and outer solar system. The dwarf planets in the Kuiper Belt record an unexpectedly large number of giant collisions, requiring a special dynamical event at the end of solar system formation.

*Subject headings:* Kuiper belt objects — individual (Haumea), methods: numerical

## 1. INTRODUCTION

The four largest dwarf planets in the Kuiper Belt form a distinct population of bodies with high albedos and volatile-rich surfaces (Schaller & Brown 2007; Stansberry et al. 2008). A significant history of collisions is suggested by the abundance of satellites in this group, which is much higher than expected for the Kuiper Belt as a whole (Brown et al. 2006). Three of the four have known satellites: Pluto has three, Haumea (formerly 2003 EL<sub>61</sub>) has two, Eris (2003 UB<sub>313</sub>) has one, and Makemake (2005 FY<sub>9</sub>) has no substantial satellite (Brown 2008). The size and orbits of these satellites are different from those found around smaller (100-km size) Kuiper Belt Objects (KBOs). To date, most known satellites around smaller KBOs are thought to have formed via a still-debated capture mechanism (Noll et al. 2008). Hence, a different satellite formation process is needed for the dwarf planets, and the most promising mechanism is collisions. Recently, numerical simulations support a giant collision origin for Pluto’s massive satellite, Charon (Canup 2005). However, the formation of the smaller satellites on the other dwarf planets has not been studied in detail.

Haumea, a  $\sim 1500$  km diameter classical belt object with a semi-major axis of 43 AU, is a particularly puzzling case as it is also associated with several smaller

KBOs with diameters between 70 and 365 km. The smaller KBOs share similar orbits and surface properties. The associated KBOs have been likened to collisionally-produced dynamically and compositionally associated “families” that are observed in the asteroid belt (Brown et al. 2007). We collectively refer to Haumea, its satellites and proposed family members as the Haumea system. Haumea has the only known family in the Kuiper Belt. The Haumea family members share a deep water spectral feature and neutral color (Brown et al. 2007; Ragozzine & Brown 2007; Schaller & Brown 2008). The water feature is unique in the Kuiper Belt (Brown et al. 2007) and indicative of unusually carbon-free water ice (Pinilla-Alonso et al. 2009).

Haumea also has the distinction of being the only known highly elongated dwarf planet though its precise shape is not known. It has a spin period of only 3.9 hours (Rabinowitz et al. 2006), the fastest of all the major and dwarf planets. The surface of Haumea is nearly homogeneous with the exception of a red spot or faint red hemisphere (Lacerda et al. 2008; Lacerda 2009); hence, the light curve is primarily a reflection of the non-spherical shape. Using the observed light curve and rotation period, Rabinowitz et al. (2006) fit a density of  $2.6 \text{ g cm}^{-3}$  assuming an equilibrium fluid body (a Jacobi ellipsoid). Although the dimensions of Haumea are not yet uniquely constrained (Lockwood & Brown 2009), the observations

require a tri-axial shape (see Table 2) (Rabinowitz et al. 2006). The derived density is greater than the average of  $\sim 2 \text{ g cm}^{-3}$  for the largest KBOs (Brown 2008), although the density may be smaller with some internal friction (Holsapple 2007).

Based on the relatively clean water ice surface and higher than average bulk density, Brown et al. (2007) argue that Haumea is differentiated with a rocky core and icy mantle. They propose that the family members and satellites are collisionally-derived fragments that originated primarily from the icy mantle. The satellites and family members are orders of magnitude less massive than Haumea, and the family members have a minimum velocity at infinity ( $V_\infty$ ) of about  $150 \text{ m s}^{-1}$  (Ragozzine & Brown 2007, 2009). The velocity dispersion is much less than expected if the Haumea family formed as the result of a catastrophic impact, as in the formation of asteroid belt families (e.g., Nesvorný et al. 2006; Michel et al. 2004). In a catastrophic disruption event, a parent body is disrupted and dispersed such that the largest remnant is less than or equal to half the original mass. In the gravity regime, the fragments have initial velocities relative to the largest remnant comparable to the escape speed ( $V_{\text{esc}}$ ) of the disrupted parent body (Benz & Asphaug 1999). Thus, the observed magnitude of the velocity dispersion ( $V_\infty$ ) of asteroid belt families is significant with respect to  $V_{\text{esc}}$  of the largest remnant; in other words,  $V_{\text{esc}}$  of the parent body was much greater than  $V_{\text{esc}}$  of the largest remnant in gravity dominated disruption events. Unlike most asteroid belt families, the velocity dispersion among Haumea family members is a small fraction of the escape velocity from Haumea ( $V_{\text{esc}} \sim 900 \text{ m s}^{-1}$ ). Based on the current models of family formation via catastrophic disruption, the Haumea family could not have formed by catastrophic disruption of a much larger parent body.

Two impact scenarios have been proposed for the formation of the Haumea system. Brown et al. (2007) proposed an impact event that falls in the catastrophic disruption category, which does not agree with the observed velocity dispersion among family members. To explain the small velocity dispersion, Schlichting & Sari (2009) suggest the breakup of a single large moon in orbit around Haumea. However, they do not provide an explanation for the initial state: a large moon in close orbit around a fast-spinning, elongated planet. To date, no known impact scenario explains all of the unusual characteristics of the Haumea system.

In this work, we quantitatively model the formation of the Haumea system. We propose that the Haumea family formed via a novel type of giant collision: a *graze and merge* impact between two comparably sized bodies resulting in high angular momentum, which spun off icy fragments that became satellites and family members. The analytic and numerical methods are described in §2. The results are presented in §3, and the implications for giant impacts in the Kuiper Belt are discussed in §4.

## 2. METHODS

To reduce the parameter space of possible collisions that produce a Haumea-like system, we used a three step process: 1) derive an analytic prediction of plausible impact parameters (§2.1); 2) conduct low-resolution simulations over a broad parameter space based on the

results of the analytic prediction (§2.2); and 3) simulate the most promising impact scenarios in high resolution (§2.3). The next three sections outline the method used in each step.

### 2.1. Analytic Prediction of Impact Parameters

Following Canup et al. (2001), using the conservation of energy and momentum, we derived an expression for the impact parameter and projectile-to-target mass ratio needed to obtain the observed angular momentum of Haumea via a giant impact. Because Haumea is rotating near its spin instability limit and the observed velocity dispersion among family members is small, we consider the case where all of the angular momentum from the collision is retained in the remaining body. Assuming that the relative velocity between the projectile and target was zero at infinity, the impact parameter,  $b$ , is given by

$$b = \frac{L}{L_{\text{crit}}} \frac{k}{\sqrt{2}f(\gamma)}, \quad (1)$$

where  $b$  is in units of the sum of the radii of the projectile and target,  $L$  is the angular momentum, and  $L_{\text{crit}} = kM^{5/3}G^{1/2}(\frac{3}{4\pi\rho})^{1/6}$ , where  $k$  is the inertial constant (2/5 for a sphere),  $M$  is the total mass, and  $\rho$  is the bulk density.  $L_{\text{crit}}$  is, therefore, the critical spin angular momentum that a spherical body with constant density can sustain. The mass ratio of projectile to the total mass,  $\gamma = \frac{M_P}{M_T + M_P}$ , enters Eq. 1 through  $f(\gamma) = \gamma(1-\gamma)(\gamma^{1/3} + (1-\gamma^{1/3}))^{1/2} \sin \theta$  where  $\theta$  is the impact angle. However, if we assume that the impact velocity is greater than  $V_{\text{esc}}$ , the total energy equation will no longer equal zero (Eq. B3 of Canup et al. 2001). In this case, the impact parameter is constrained by

$$b = \frac{L}{L_{\text{crit}}} \frac{k}{\sqrt{2}f(\gamma)} \frac{V_{\text{esc}}}{V_i}, \quad (2)$$

where  $V_i$  is the impact velocity and  $V_{\text{esc}}$  is the mutual escape velocity (Eq. 1 of Canup 2005).

For Haumea we assume a mass of  $4.2 \times 10^{21} \text{ kg}$  and a spin period 3.92 hr from Rabinowitz et al. (2006). Using these values,  $\frac{L}{L_{\text{crit}}}$  ranges between 1.1 and 0.8 for a plausible range of bulk densities of the colliding bodies ( $1.5$  to  $2.5 \text{ g cm}^{-3}$ ). The results from Eq. 1 and 2 are shown in Fig. 1.

If the impact velocity equals the mutual escape velocity of the projectile and target, Eq. 1 requires an impact parameter close to one ( $> 0.8$ ) and a projectile close to the mass of the target in order to attain the angular momentum in Haumea (Fig. 1). Increasing the bulk density of the bodies broadens the range of impact parameters that could transfer the observed angular momentum. Similarly, when  $V_i > V_{\text{esc}}$ , there is a larger range of possible projectile-to-target mass ratios that could produce the angular momentum of Haumea (Eq. 2, dotted line in Fig. 1 assumes the mean bulk density for large KBOs of  $2 \text{ g cm}^{-3}$ ). This work assumes no initial spin in the target and projectile. Initial spin in the same sense as the spin angular momentum would potentially increase the range of mass ratio that could produce a Haumea-like remnant.

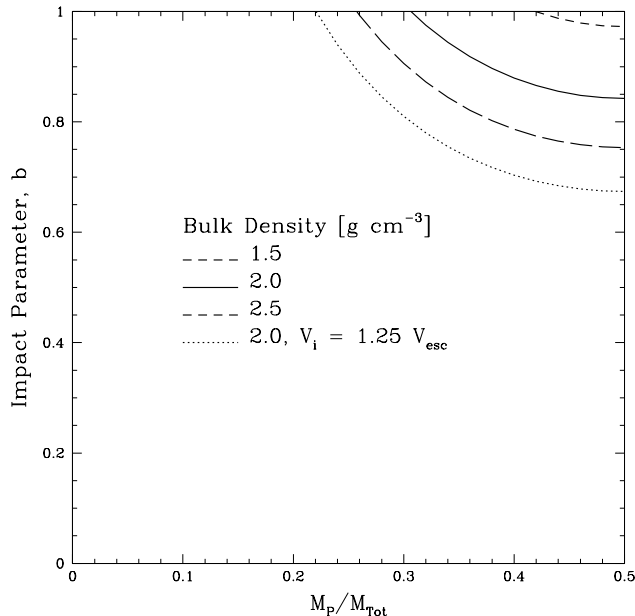


FIG. 1.— Analytic prediction of impact scenarios leading to the angular momentum of Haumea for various bulk densities and  $V_i$ . Solutions are lines as a function of impact parameter,  $b$ , and mass of the projectile normalized by the total mass,  $M_P/M_{Tot}$ . For  $V_i = V_{esc}$  (Eq. 1) the short dashed, solid, and long dashed lines show solutions for bulk densities of 1.5, 2.0, and 2.5  $\text{g cm}^{-3}$ , respectively. For  $V_i = 1.25V_{esc}$  (Eq. 2) the dotted line shows solutions for a bulk density of 2.0  $\text{g cm}^{-3}$ . Haumea parameters are taken from Rabinowitz et al. (2006).

As the impact velocity increases, the remaining body does not retain most of the angular momentum of the encounter, as is assumed in the equations above. When the impact velocity is large enough to begin to disrupt the target ( $3 - 3.5 \text{ km s}^{-1}$ , Stewart & Leinhardt 2009), a significant amount of angular momentum will be carried away by the smallest fragments (see Fig. 2 in Leinhardt et al. 2000). Compensating for the partial loss of angular momentum by further increasing the impact velocity will lead to the catastrophic disruption regime. Recall that the catastrophic disruption regime is ruled out based on the velocity dispersion among the family members. Although the angular momentum distribution in the catastrophic regime has not been extensively studied, we expect that angular momentum transfer to the largest remnant is inefficient. The largest remnant is a gravitationally reaccumulated body; hence, the angular momentum of the reaccumulated mass does not approach the spin instability limit. Numerical simulations of catastrophic disruption that resolve the shape of the largest remnant produce spherical remnants not fast spinning elongated remnants (Leinhardt et al. 2000; Leinhardt & Stewart 2009).

Thus, the analytic argument suggests that the most straightforward way to create a body with high angular momentum via a collision is in a grazing impact between two objects of similar size at a velocity close to the mutual escape speed. Note, however, that the analytic solution makes several assumptions. For example, mass that is lost from the system as a result of the collision is not taken into account. The escaping mass carries away some energy and momentum. In addition, the energy and momentum conservation are approximated and do

not include terms for energy lost in heat and fracturing of the target and projectile.

## 2.2. Low Resolution Simulations

To examine the predictions of the idealized analytic solutions, we conducted a series of low-resolution simulations of impacts between gravitational aggregates (Table 1). Because the encounter velocities are modest ( $\leq 1.2 \text{ km s}^{-1}$ ), the energy lost to shock deformation during the collision is minimal, and gravitational forces dominate. Thus, for efficiency, the low-resolution simulations utilized the  $N$ -body gravity code **pkdgrav**, which resolves inelastic particle-particle collisions (Richardson et al. 2000; Leinhardt et al. 2000; Leinhardt & Richardson 2002). Particle collisions were modeled using a hard sphere model, where the unbreakable spherical particles are non-penetrating. The outcome of each inelastic collision were governed by conservation of momentum and typical coefficients of restitution of 0.5 and 1.0 in the normal and tangential directions, respectively, for particles representing ice or rock (see discussion in Leinhardt & Stewart 2009).

Each projectile and target was modeled as a rubble pile, a gravitationally bound aggregate of 955 particles with no tensile strength (Leinhardt et al. 2000; Leinhardt & Richardson 2002). Previous simulations (Leinhardt et al. 2000) show that a thousand particles is enough to resolve general shape features in a rubble pile. We assumed two internal configurations: homogeneous and differentiated bodies. In the differentiated cases, the colliding bodies had two layers: a  $1.0 \text{ g cm}^{-3}$  mantle representing ice and a  $3.0 \text{ g cm}^{-3}$  core representing rock. The mass ratio of the icy mantle to rocky core was also varied to reach the desired bulk density, which resulted in a range of initial radii from about 500 to 800 km.

Based on the analytic solutions, the projectile-to-target mass ratio was assumed to be one in most cases with a subset of simulations considering  $M_P/M_T = 0.5$ . The parameter space included initial bulk densities from  $1.0$  to  $3.0 \text{ g cm}^{-3}$ , impact velocities between  $0.7$  to  $1.2 \text{ km s}^{-1}$ , impact parameters from  $0.55$  to  $0.71$ , and total system masses of  $4.5$  to  $8.2 \times 10^{21} \text{ kg}$ .

Due to the low resolution, each individual particle had relatively large mass, and it was difficult to strip material from the surface of the largest remnant. As a result, we use these simulations only to refine the impact parameters that reproduce the observed rotation period and approximate mass of Haumea. The calculated mass of the largest remnant will be biased slightly upward, and the family members will be completely unresolved.

## 2.3. High Resolution Simulations

Based on the low-resolution simulation results, impact parameters were chosen for high-resolution calculations of the formation of Haumea and its family members (Table 2). We used a hybrid hydrocode to  $N$ -body code technique similar to the method used in studies of catastrophic collisions in the asteroid belt and the outer solar system (eg. Michel et al. 2003; Durda et al. 2004; Nesvorný et al. 2006; Leinhardt & Stewart 2009). The hybrid technique captures the shock deformation during the early stage of the collision and follows the gravity-controlled evolution of the material to very late times.

We used GADGET (Springel 2005), a smoothed particle hydrodynamics code (SPH) modified to use tabular equations of state (Marcus et al. 2009), for the hydrocode phase and **pkdgrav** for the gravity phase of the calculation.

SPH is a Lagrangian technique for solving the hydrodynamic equations in which the mass distribution is represented by spherically symmetric overlapping particles that are evolved with time (Gingold & Monaghan 1977; Lucy 1977). SPH has been used extensively to model impacts in the solar system from asteroid collisions and family forming events to the formation of the Pluto-Charon system (e.g. Asphaug et al. 1998; Michel et al. 2003; Canup 2005). Although GADGET includes self-gravity it is not practical to use a hydrocode for the entire integration of the collision as the timestep is limited by the Courant condition.

The targets and impactors were differentiated bodies composed of an ice mantle over a rock core with a bulk density of  $\sim 2 \text{ g cm}^{-3}$ . The largest KBOs have bulk densities of about  $2 \text{ g cm}^{-3}$ , which is similar to the density predicted from cosmochemical estimates of the rock to ice ratio in the outer solar system (McKinnon et al. 1997, 2008). Although the internal structures of large KBOs are unknown (Leinhardt et al. 2008), strong water features on the surfaces of the largest bodies suggest that they have differentiated (McKinnon et al. 2008). Hence, in this work, we consider collisions between differentiated bodies only in the high resolution simulations.

The material in the rocky cores were modeled using a tabulated version of the molecular ANEOS equation of state for  $\text{SiO}_2$  (Melosh 2007), and the ice mantles were modeled with the tabular 5-Phase equation of state for  $\text{H}_2\text{O}$  (Senft & Stewart 2008). The internal temperature profile is dependent on the ice to rock ratio and the viscosity of ice; models indicate that temperatures for a Charon size body are generally low (e.g.,  $< 300 \text{ K}$  after 4 Ga McKinnon et al. 2008). As a result, a constant initial temperature of  $150 \text{ K}$  was chosen. The bodies were initialized with hydrostatic pressure profiles. They were then allowed to settle in isolation for many dynamical times at which point all particles have negligible velocities ( $\text{cms s}^{-1}$ ) at the specified temperature. The number of particles ranged from  $\sim 1.2 \times 10^5$  to  $\sim 4 \times 10^5$  ( $\sim 24\text{--}36$  particles per target radius) a sufficient resolution to resolve shock heating and the formation of family members, and the results were checked for sensitivity to resolution. As in all previous studies of giant impacts, the materials are hydrodynamic (see discussion in §3.3).

The GADGET simulations were run as long as was practically feasible, normally about 60 simulation hours. At this time, the collision and mass loss process was complete; however, more time was needed to determine the long-term orbital stability of material bound to the largest object.

### 2.3.1. Orbital Evolution of Collision Fragments

The N-body code **pkdgrav** was used to integrate the orbiting fragments for thousands of spin periods of the largest remnant. The GADGET output was translated and handed off to **pkdgrav**. In previous work on asteroid family formation, pairs of **pkdgrav** particles were merged into a single particle after each particle-particle collision to reduce computation time (resulting in arti-

cial perfectly spherical collision remnants). In this work, because of the significant elongation in the largest remnant, the shape and rotation rate needed to be preserved for the orbital evolution calculation, and particle merging could not be used. Hence, the **pkdgrav** calculation utilized inelastic collisions (§2.2) to preserve the shape and gravitational potential of the largest remnant.

However, the number of particles in the largest remnant in the GADGET simulation ( $\sim 10^5$  particles) is too large to integrate in **pkdgrav** because of the computational expense of calculating the collisions within the largest remnant. Therefore, the largest remnant was de-resolved to contain  $\sim 10^3$  particles by placing a grid over the body and placing all particles within a grid cell into a single particle. Each merged particle had a mass equal to the combined mass, a position equal to the center of mass position, and velocity vector equal to the center of mass velocity. The spin and shape of the largest remnant was preserved. The mass of the largest remnant using inelastic collisions was compared with a perfect merging collision outcome to test the stability of the handoff. The mass of the largest remnant was very similar in both cases.

The shape and ice-to-rock ratio of individual smaller remnants (the satellites and family members) were not resolved in the SPH simulation. Hence, the self-gravitating remnants outside of the largest remnant were merged into single particles. In this manner, the de-resolved **pkdgrav** calculation allowed the stability simulation to run for thousands of orbits in a reasonable amount of time.

## 3. RESULTS

### 3.1. A Collision Scenario for the Haumea System

The impact conditions and outcomes of the low-resolution numerical simulations of possible Haumea-forming impact events are summarized in Table 1. The last column of the table, collision type, describes the general class of the collision. We found three different collision outcomes in our restricted parameter space (see §4 for further discussion): 1) *merge* – the projectile and target merge after initial impact with little or no mass loss; 2) *graze & merge* – the projectile initially hits the target with a large impact parameter and then separates, the projectile is decelerated, but remains relatively intact, and subsequently recollides at a much slower velocity resulting in a merger and a fast-spinning body; 3) *graze & run* – the projectile and target hit but do not lose enough energy to remain bound to each other.

The impact parameters that produced elongated bodies with a total mass and spin period similar to Haumea tend to be of the graze and merge category. Thus, collisions that form a Haumea-like body are found in a distinctly different parameter space than catastrophic disruption events.

High-resolution hybrid simulations of the most successful collision scenarios for forming a Haumea-like planet were conducted to investigate the properties of the satellites and family members (Table 2). A time series from an example collision simulation (sim. 4) is presented in Fig. 2, which displays the materials in cross-section looking down on the collision plane. The last frame, which has been rotated by ninety degrees to show the collision

TABLE 1  
SUMMARY OF PARAMETERS AND RESULTS FROM SELECTED PKDGRAV SIMULATIONS.

$R$ km	$\frac{M_P}{M_T}$	$\rho_b$ g/cm <sup>3</sup>	$\frac{\rho_c}{\rho_m}$	$b$ –	$V$ km/s	$\frac{M_{lr}}{M_{Tot}}$	semi-axes of lr km×km×km	$\rho_{lr}$ g/cm <sup>3</sup>	$P_{lr}$ hr	Collision Type
770	0.5	2.0	1.0	0.80	0.7	0.98	1270×750×690 <sup>b</sup>	1.6	4.4	merge
770	0.5	2.0	1.0	0.80	0.8	0.88	1000×708×670	2.0	5.0	graze & merge
770	0.5	2.0	1.0	0.80	0.9					graze & run
650	1.0	2.0	1.0	0.65	0.8	0.99	1396×711×632	1.7	4.9	merge
650	1.0	2.0	1.0	0.65	0.9	0.99	1398×750×670	1.5	5.0	graze & merge
650	1.0	2.0	1.0	0.65	1.0					graze & run
800	1.0	1.0	1.0	0.6	1.0					graze & run
650	1.0	2.0	3.0	0.6	1.0					graze & run
630	1.0	2.6	3.0	0.6	1.0	0.99	1270×657×607	2.1	3.8	graze & merge
580	1.0	3.3	3.0	0.6	1.0	0.99	1164×606×526	2.8	3.7	graze & merge
650	1.0	2.0	3.0	0.55	0.7	0.99	1219×717×699	1.8	4.1	merge
650	1.0	2.0	3.0	0.55	0.8	0.99	1293×692×666	1.8	4.3	merge
650	1.0	2.0	3.0	0.55	0.9	0.99	1385×680×634	1.8	4.2	merge
650	1.0	2.0	3.0	0.55	1.0	0.99	1362×708×647	1.7	4.5	graze & merge
650	1.0	2.0	3.0	0.55	1.1					graze & run
650	1.0	2.0	3.0	0.55	1.2					graze & run
650	1.0	2.0	3.0	0.60	0.8	0.99	1303×702×688	1.7	4.1	merge
650	1.0	2.0	3.0	0.60	0.9	0.99	1322×446×636	1.7	3.9	graze & merge
650	1.0	2.0	3.0	0.60	1.0					graze & run
650	1.0	2.0	3.0	0.65	0.7	0.99	1252×740×672	1.7	4.1	merge
650	1.0	2.0	3.0	0.65	0.8	0.99	1273×698×697	1.7	4.2	graze & merge
650	1.0	2.0	3.0	0.65	0.9	0.99	1445×699×648	1.6	4.9	graze & graze & merge

<sup>a</sup> $R$  – radius of target;  $\frac{M_P}{M_T}$  – mass of projectile normalized by mass of target;  $\rho_b$ ,  $\rho_c/\rho_m$  – bulk density, density ratio of core to mantle; for  $\rho_c/\rho_m > 1.0$ ,  $\rho_c = 3.0$  and  $\rho_m = 1.0$  g cm<sup>−3</sup>;  $b$  – impact parameter;  $V$  – first impact velocity;  $M_{lr}/M_{Tot}$  – mass of largest remnant normalized by total mass;  $\rho_{lr}$  – bulk density of lr;  $P_{lr}$  – spin period of lr. In all cases, each body contained 955 particles and  $M_{Tot} = 4.5 \times 10^{21}$  kg. Bulk density, calculated by circumscribing all particles within an axisymmetric ellipsoid, is always a minimum value.

<sup>b</sup>lr is significantly non-axisymmetric.

outcome edge-on, shows the surfaces of the largest remnant and the debris field. During the collision, the rocky cores of the progenitor bodies merge, and the resulting primary body spins so quickly that it sheds icy mantle material from the ends in many small clumps. Some of this material is gravitationally bound and some escapes from the primary. In this scenario, the satellites and family members do not originate from the initial contact; instead, they are spun off after the subsequent merger. As a result, the  $V_\infty$  of the family members are small; in other words, the ejection velocities of the fragments are not much greater than the escape velocity of the merged primary.

The analytic and numerical results show that the optimum parameter space to form a Haumea-like planet is in an encounter slightly more energetic than merging between comparably sized bodies. Some of the merging cases that are close to the transition to graze and merge also produce an elongated, fast-spinning largest remnant; however, from high-resolution simulations, we find that such merging simulations eject less mass and, thus, do not tend to form families. Although the long-term relaxation of the bodies is not considered here, we note that impacts with a mass ratio less than one produced initially nonsymmetric largest remnants that are not consistent with observations.

The collision parameters that achieve the best agreement with observations fall in a narrow parameter space: an impact speed of 800–900 m s<sup>−1</sup> and an impact parameter between 0.6 and 0.65 for equal mass progenitors with bulk densities of 2 g cm<sup>−3</sup>. At higher impact velocities or higher impact parameters, the two bodies escape from

each other after the impact. At lower impact velocities or lower impact parameters, the two bodies merge and less material is ejected as potential family members. Initial spin would increase or decrease the impact parameter needed to achieve the same total angular momentum, as shown in idealized cases in Leinhardt et al. (2000).

### 3.2. Properties of the Satellites and Family

The impact conditions defined above reproduce the mass, spin period and elongation of Haumea, as well as the mass and velocity distributions of the observed satellites and family members. In Fig. 3A, the observed family (triangles and dotted line from Ragozzine & Brown 2007) are normalized to the number of resolved fragments in sim. 4 after 2000 spin orbits to facilitate comparison. Unresolved fragments have too few particles ( $N < 10$ ) at handoff to be numerically resolved. Haumea and the two known satellites are indicated by filled triangles. The diameter of Haumea family members was derived from the absolute magnitude assuming similar albedo to Haumea of  $\sim 0.7$ , and the diameter was converted into mass assuming a bulk density of 1 g cm<sup>−3</sup> for a primarily ice composition. In Fig. 3B, the open triangles below zero indicate the minimum relative velocities of the known family members with respect to the center of the family using the reconstructed position for Haumea (Ragozzine & Brown 2007).

As shown in Fig. 3B, the total mass of potential satellites and family members is small:  $< 0.07M_{lr}$  for sim. 1–4 from Table 2. Although the modeled mass is larger than the known satellites and family members ( $\sim 0.01M_{lr}$ ), one does not expect that all of these bodies have been

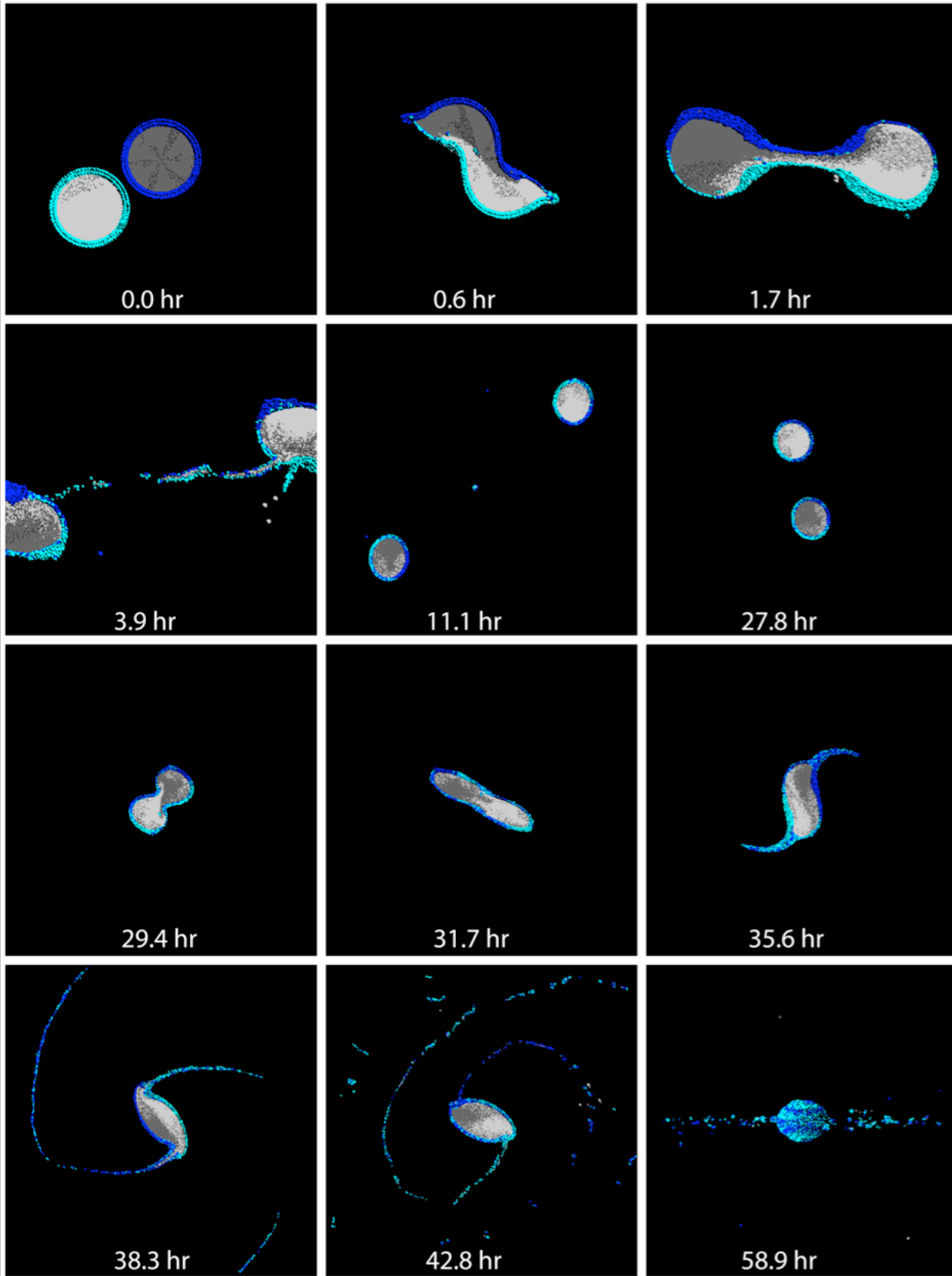


FIG. 2.— Time series of a graze and merge event: 650-km diameter bodies colliding at  $900 \text{ m s}^{-1}$  with an impact parameter of 0.6 (sim. 4 in Table 2). Cross section view through the collision plane which is in the page. Field of view is initially  $5000 \times 5000 \text{ km}$ , increasing to  $10000 \times 10000 \text{ km}$  at 11.1 hours. The last frame (58.9 hrs) shows the system edge on. Color denotes the provenance of the materials: icy mantles (cyan and blue) and rocky cores (light and dark grey). For visual clarity in the last frame, the radius of each dot equals one fifth of the smoothing length of the corresponding SPH particle, for all other frames the dots are point particles. Although some material is exchanged during the first impact, each body remains largely intact after separation. The rocky cores merge after the second impact, forming a differentiated primary. The surface of the merged body has distinct patches of ice that originate from each of the precursor bodies. The fragments thrown from the merged body are primarily material from the icy mantles. An animation is available in the online version of the Journal.

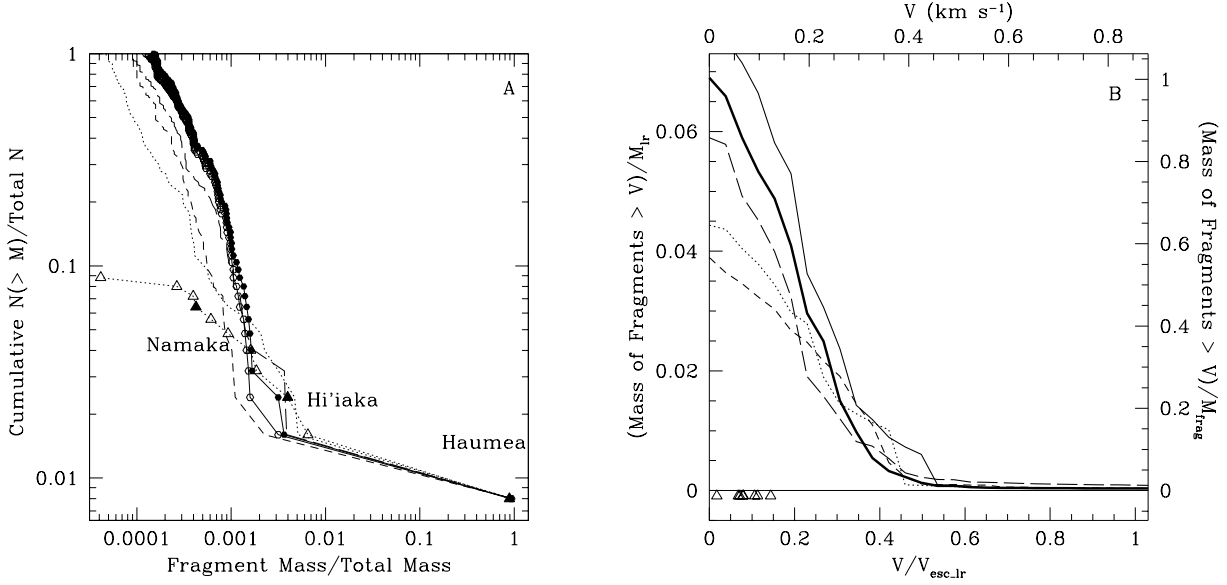


FIG. 3.— Mass and velocity distributions for simulations 1-4 in Table 2. (A) Cumulative number of resolved fragments larger than mass  $M$  versus fragment mass (short dash, dotted, long dash, and filled circles are results from sim. 1-4 after  $\sim 100$  orbits, the open circles are results from sim. 4 after  $\sim 2000$  orbits). Triangles and dotted line are the observed family normalized to sim. 4. (B) Cumulative velocity distribution of fragments (short dashed, dotted, long dashed, and thin solid line, sim. 1-4, respectively, after 100 orbits, thick black line is from sim. 4 after 2000 orbits). The lower abscissa is normalized by the escape speed from the largest remnant (model Haumea). The left ordinate is the mass of fragments with relative velocities greater than  $V$  normalized by the mass of the largest remnant, and the right ordinate is normalized by the total mass in smaller fragments in long running sim. 4. Open triangles below zero are minimum relative velocities of family members.

TABLE 2  
SUMMARY OF HAUMEA FAMILY FORMING SIMULATION RESULTS AND OBSERVATIONS.

Sim. No.	$M_T$ $10^{21}$ kg	$R_T$ km	$\mu$	$b$	$V_{\text{imp1}}$ $\text{m s}^{-1}$	$V_{\text{imp2}}$ $\text{m s}^{-1}$	$M_{\text{lr}}$ $10^{21}$ kg	$\rho_{\text{lr}}$ $\text{g cm}^{-3}$	semi-axes of lr km $\times$ km $\times$ km	$P_{\text{lr}}$ hr	$f_{\text{H}_2\text{O}}$
1	2.25	650	1	0.6	800	260	4.3	2.2	$960 \times 870 \times 640$	3.6	0.86
2 <sup>b</sup>	2.25	650	1	0.6	800	240	4.3	2.1	$1090 \times 820 \times 680$	3.4	0.79
3	2.25	650	1	0.65	800	280	4.3	2.2	$1100 \times 940 \times 640$	3.7	0.73
4	2.25	650	1	0.6	900	260	4.2	2.1	$1100 \times 810 \times 620$	3.9	0.80
5 <sup>c</sup>	4.80	830	0.22	0.71	3000	-	4.64	2.3	$1700 \times 1500 \times 1500$	28	-
Obs. <sup>d</sup>	-	-	-	-	-	-	4.006	2.6	$1000 \times 750 \times 500$	3.9	-

<sup>a</sup> $M_T$  – mass of target body;  $R_T$  – radius of target body;  $\mu$  – mass ratio of projectile to target;  $b$  – impact parameter;  $V_{\text{imp1}}$  – first impact velocity;  $V_{\text{imp2}}$  – second impact velocity in graze and merge event;  $M_{\text{lr}}$  – mass of largest remnant;  $\rho_{\text{lr}}$  – bulk density of lr;  $P_{\text{lr}}$  – spin period of lr;  $f_{\text{H}_2\text{O}}$  – ice mass fraction of all smaller fragments.  $\rho_{\text{lr}}$  and  $f_{\text{H}_2\text{O}}$  from end of hydrocode phase (50–60 hrs); all other simulation results from end of gravity phase ( $\sim 100$  orbits).

<sup>b</sup>Higher resolution version of sim. 1 ( $N = 4 \times 10^5$ ).

<sup>c</sup>Proposed impact scenario from Brown et al. (2007).

<sup>d</sup>Observed characteristics of Haumea (Ragozzine & Brown 2009; Rabinowitz et al. 2006). Note: simulations presented here attempted to match the mass of  $4.21 \pm 0.1 \times 10^{21}$  kg quoted in Rabinowitz et al. (2006).

observed or that all should survive to the present day. Hence, the modeled mass of smaller bodies is consistent with the observed Haumea system. In addition, the masses of individual satellite and family members are small, with most  $< 10^{-3} M_{\text{Ir}}$ , which is also in agreement with the observed family (Fig. 3A).

Almost all of the family members have a relative velocity that is  $< 0.5V_{\text{esc}}$  with respect to the primary, with 80-90% of the mass having a speed  $< 300 \text{ m s}^{-1}$  and 35-60% of the mass having a speed less than  $150 \text{ m s}^{-1}$ . Note that  $150 \text{ m s}^{-1}$  is the *minimum* velocity dispersion of the observed family; the true values could be about two times larger when accounting for the unknown orbital orientation (Ragozzine & Brown 2007). The model predicts that negligible mass reaches the typical velocity dispersion among 100-km size KBOs of about  $1000 \text{ m s}^{-1}$ .

As a resolution test one simulation was completed at higher resolution (no. 2, dotted line in Fig. 3,  $N = 4 \times 10^5$  compared to  $N = 1.2 \times 10^5$  for simulations 1, 3 - 5) with the same collision parameters as sim. 1. The number and velocity dispersion of the remnants are consistent with the lower resolution simulations thus we are confident we have reached resolution convergence.

The modeled satellite and family members are comprised almost entirely of icy mantle material (73-86% by mass). The bulk density of the largest remnant increases by  $\sim 10\%$  over the initial density of the progenitor bodies as a result of the preferential stripping of the lower-density ice mantle (Fig. 2). The modeled bulk density of the largest remnant is within the range of uncertainty for the density of Haumea. These results explain the shared water ice spectral feature of the bodies in the Haumea system and the complete lack of bodies with a similar water ice spectrum in the general (not dynamically associated) KBO population around Haumea. Negligible mass was dispersed into the background KBO population in the graze and merge family-forming event.

In one simulation (no. 4), the orbits of the satellites and family members were integrated for 2000 spin orbits to assess the stability of the newly formed system around the elongated primary. At this time, there are  $\sim 35$  objects gravitationally bound and in orbit about the primary (the mass in orbit is about  $0.01 M_{\text{Ir}}$  and the mass in family members is about  $0.06 M_{\text{Ir}}$ ). These bodies have eccentricities below 0.9 and instantaneous orbits that do not intersect the primary. The bound objects and instantaneous orbital parameters were determined using the `companion` code (Leinhardt & Richardson 2005). Here, we do not assess the longer term dynamical evolution of the collisional system. However, we demonstrate that some bodies remain in stable orbits around the elongated, fast-spinning primary well after the collision event. Unlike previously thought (Brown et al. 2006), the formation of multiple small satellites around Haumea does not require accretion in a massive disk.

### 3.3. The Effect of Material Strength

Simulations of giant impact events usually utilize a SPH code (e.g., this work, Benz et al. 1986, 1988; Canup 2004, 2005; Benz et al. 2007; Marinova et al. 2008). A Lagrangian SPH calculation has the advantages of an arbitrarily large spatial domain and efficiency in tracking small fragments. In an Eulerian (grid-based) code, the spatial domain must be decided upon in advance

and tracking small fragments through the mesh is computationally very expensive. In previous studies, giant impact calculations have neglected material strength on the grounds that self-gravitational forces and shock pressure gradients dominate the problem. Most giant impact studies have focused on the end stages of planet formation and considered hypervelocity impact events that generate strong shock waves. Hence, it has been reasonable to neglect material strength. For collisions between dwarf planets at subsonic velocities, however, it is not obvious that strength can be neglected.

We conducted a few comparison three-dimensional simulations using the Eulerian shock physics code CTH (McGlaun et al. 1990) with adaptive mesh refinement (Crawford 1999). CTH has the option to include self-gravitational forces using the parallel tree method of (Barnes & Hut 1986). The simulations had a resolution of 31 to 42 km (30 to 40 cells across each initial body). In the nominal simulations, each CTH cell is comparable in physical size to a single GADGET particle within the initial bodies, although the effective resolution in CTH is slightly higher because of the differences in smoothing lengths between the two codes. Tests at twice the resolution (in each dimension) yielded similar results. The CTH calculations utilize the same tabulated equation of state models as used in the GADGET SPH simulations. Each body was initialized in gravitational equilibrium at a constant temperature of 150 K. The radii were 650 km, with an ice mantle over a rock core such that the bulk density was  $2 \text{ g cm}^{-3}$ . To allow for reasonable calculation times, material in cells with a bulk density less than  $0.01 \text{ g cm}^{-3}$  was discarded from the calculation. Hence, fragments that become the moons and family members of Haumea are not modeled in CTH. Only the formation of the primary (Haumea) is considered.

Some simulations were hydrodynamic (no shear strength) for direct comparison to GADGET. Other simulations utilized a simple friction law (the geological yield model in CTH) that represents friction in fractured (damaged) ice (Senft & Stewart 2008):  $Y_0 + \mu P$ , where  $Y_0 = 0.1 \text{ MPa}$  is the cohesion,  $\mu = 0.55$  is the friction coefficient, and  $P$  is pressure. The shear strength is limited to a maximum of 0.1 GPa. Shear strength is thermally degraded as the temperature approaches 273 K. The tensile strength was 1.7 MPa. For simplicity, the same strength model was used in both the ice and rock components. The strength parameters are similar to models of sedimentary rocks (e.g., Collins et al. 2008), which are significantly weaker than crystalline rocks.

Because the CTH calculations require significantly more computational time than the GADGET calculations, comparisons between the two codes were made at early stages in the impact event. Hydrodynamic CTH calculations are similar to the GADGET results (Fig. 4). The minor differences at late times are due to small differences in the initial conditions: the initial separation of the bodies and the better resolution of the ice-rock interface in CTH.

In cases with strength, a number of differences are observed. The radial oscillations in each body after the initial contact are not observed with strength. These oscillations arise from momentum transfer between the rock core and ice mantle; the difference in particle velocities from the momentum transfer is damped with strength.



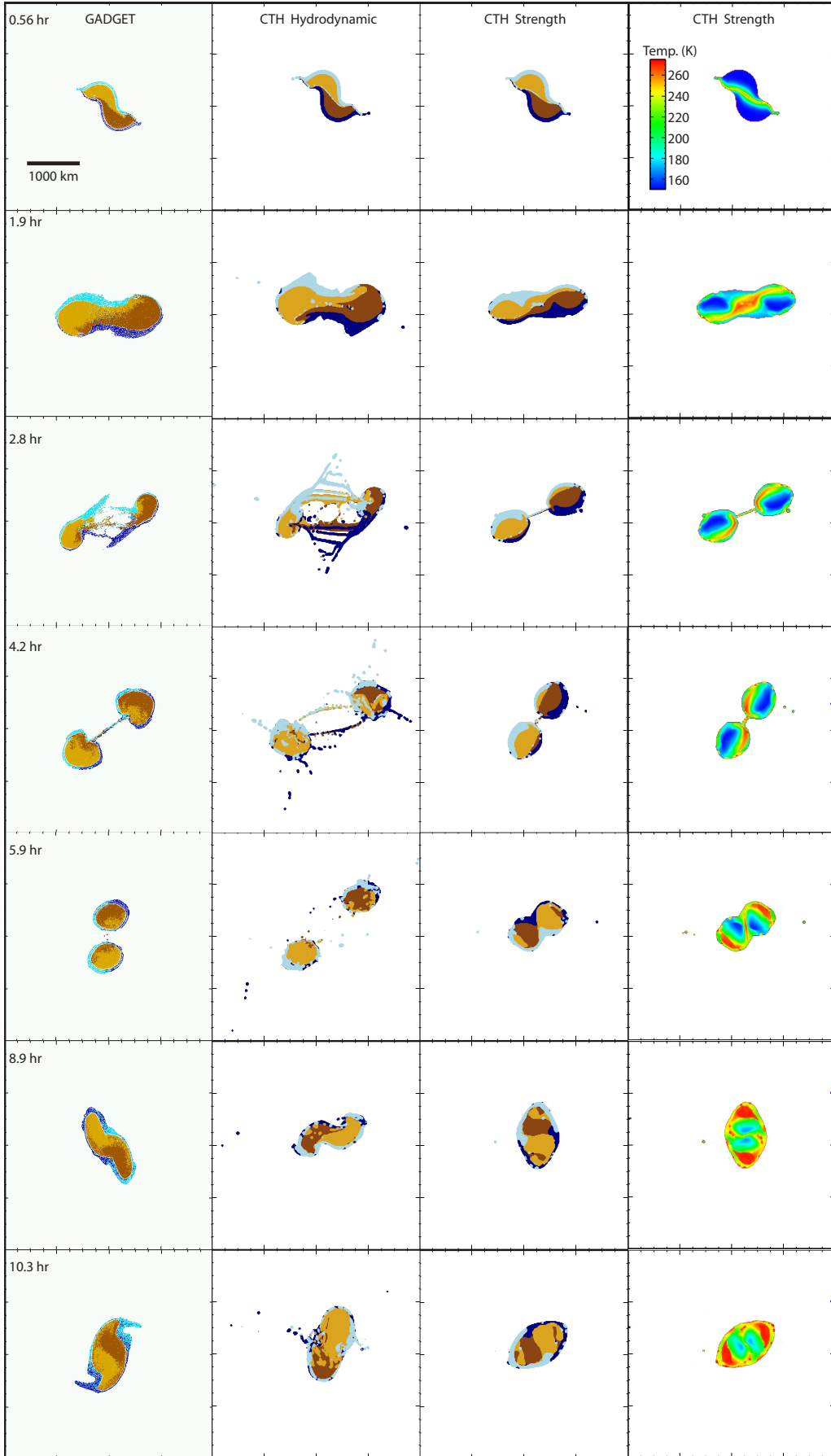


FIG. 4.— Time series of sim. 1 in Table 2 using GADGET and CTH with and without strength. View of the cross section through the impact plane. Each panel is  $4000 \times 4000$  km. Columns 1-3: Colors represent material (blues – ice mantles; browns – rock cores). Column 4: Color represents temperature.

The number of ‘strings of fragments’ between the two bodies after the initial contact is decreased with strength (2.8 hours in Fig. 4). Because of dissipation of energy in mechanical work during the first contact, the second contact occurs sooner with strength. The temperature increase from the impact is higher with strength because of dissipation of mechanical work as heat. Note that with and without strength, the cores of the two bodies merge quickly after the second contact. The purpose of the CTH calculation is not to try to develop a realistic strength model for large KBOs, but simply to demonstrate that the addition of a reasonable amount of internal friction yields essentially the same result as in the detailed hydrodynamic simulations.

#### 3.4. Impact-induced Heating and the Icy Surface

During the impact event, the temperature in the portions of the ice mantle in the regions of contact are raised to the phase boundary (melting or vaporization, depending on the local pressure, Fig. 4). However, negligible mass of ice is melted or vaporized. For the  $\sim 1 \text{ km s}^{-1}$  impact velocities considered here and a wide range of initial temperatures, ice that experiences the peak shock pressures will be raised to the melting or vaporization curve (Stewart et al. 2008). However, no ice is expected to completely melt or vaporize. Thus, the outcome of the collision event is not sensitive to the initial temperature as neither the rock nor ice components experience significant shock-induced phase changes during the collision event. As a confirmation, a test SPH simulation with a high temperature rock interior yielded essentially the same result.

In a graze and merge impact, the ice mantles experience severe deformation that is expected to fragment the ice. Upon merging, solid state differentiation occurs quickly, even with some strength. The surface of the resulting primary (Haumea) is covered with ice fragments that have been heated over a wide range: from negligibly to the phase boundaries. The fragmented ice mantle has negligible cohesion and may be likened to a slurry. Ice has exceedingly low friction when warm and at modest slip velocities which are exceeded in the scenario considered here (Maeno et al. 2003). Thus, we conclude that the ice mantle will have negligible resistance to mass loss due to the high angular momentum of the merged body.

Because the graze and merge portions of the impact event are similar in the GADGET and CTH calculations (with and without strength), we argue that the spin off of ice fragments at the end stages of the event is reasonably modeled in the hydrodynamic GADGET calculations.

One of the remarkable characteristics of Haumea, its larger satellite, and its family members is the strong water ice spectral feature. The graze and merge family forming event explains the ice-dominated surfaces of the Haumea system. Although the simulations cannot address the details of ice separation from other phases, the results suggest that the formation event produced an icy surface that is cleaner compared to other KBOs, as is observed (Pinilla-Alonso et al. 2009). A relatively clean icy mantle is necessary to prevent reddening from cosmic irradiation (Rabinowitz et al. 2008) over the time since the impact event ( $> 1 \text{ Ga}$ , Ragozzine & Brown 2007). Because the surface of Haumea appears so homogeneous and unlike other KBOs, we argue that it is unlikely

that the surfaces of the precursor bodies were so similar. Hence, the strong ice feature on the Haumea family must be related to the family-forming impact event.

#### 3.5. Additional Formation Scenarios

Brown et al. (2007) suggested a possible impact scenario to produce the Haumea collisional family based on numerical studies of asteroidal family forming events (Benz & Asphaug 1999): impact of a projectile with 0.22 the mass of the target at  $3 \text{ km s}^{-1}$  at an impact parameter of 0.71. The authors suggested that such an impact would both strip off a portion of the target’s mantle and impart a high spin period. We conducted a high-resolution simulation of the proposed impact scenario. Our results demonstrate that there is not enough energy and momentum coupling between the projectile and the target to produce a fast-spinning primary (sim. 5 in Table 2). The projectile shaves off some of the target material and escapes from the system, but the remaining angular momentum is insufficient to elongate the target body. Based on our analytic calculations and numerical results, it is not favorable for a small, fast projectile to impart enough angular momentum to create a fast-spinning elongated body.

Using an order of magnitude analysis, Schlichting & Sari (2009) suggest a different Haumea family forming scenario involving a two stage formation process. First, a giant impact creates an elongated fast-spinning primary and a large, tightly-bound satellite. Second, a subsequent impact onto the satellite, disrupts it and creates the family members and small satellites. Based on numerical simulations, an elongated and fast spinning primary is only produced in a slow collision with a large impact parameter and a mass ratio close to unity (Table 1, Leinhardt et al. 2000; Leinhardt & Richardson 2002); furthermore, these scenarios do not create a large tightly-bound satellite. Impact events that produce a large tightly-bound satellite (e.g., Canup 2005) do not form elongated primaries.

We have not completed an exhaustive parameter space study of family-forming collisions in the Kuiper Belt. It is possible that additional collisional scenarios such as graze and run could form the Haumea collisional family. Future work on this scenario would need to address the homogenization of the entire surface of Haumea (since it would not all melt as a result of the encounter) and the probabilities of the encounter providing enough angular momentum to a Haumea-sized target. In addition, a graze and run collision deposits only a small amount of internal energy into the target - not enough to differentiate the body. Here we present the first fully self-consistent formation model that does not require unusual pre-impact conditions.

## 4. DISCUSSION

Giant impacts are common in the late stages of planet formation, and several outcomes are possible. With approximately decreasing impact energy, a giant impact leads to: (i) *catastrophic disruption* (half or more of the target mass is lost, Benz & Asphaug 1999; Stewart & Leinhardt 2009; Marcus et al. 2009). The largest remnants are aggregates of gravitationally reaccumulated material; it is the formation mechanism for asteroid belt families. (ii) *graze and run* (a.k.a. hit and run, Asphaug

et al. 2006). In some oblique impacts, the projectile hits and then escapes the target with both bodies remaining largely intact. Note that we prefer the term “graze” rather than “hit” to indicate the need for an oblique impact. (iii) *graze and capture*. The projectile obliquely hits the target and separates, but does not have enough energy to escape and is captured in orbit. It is the favored formation mechanism for the Pluto-Charon binary (Canup 2005). (iv) *graze and merge*. The projectile obliquely hits, separates, and then recollides and merges with the target. The high angular momentum of the merged body spins off some material. Such a scenario explains the unusual characteristics of the Haumea collisional family. In an alternate scenario, a graze and merge impact to form Pluto may also produce a disk of bound material of the mass of Charon (Canup 2005). (v) *merge*. The projectile and target merge during the first contact; in some cases, a small fraction of material may be thrown into orbit or escape. The Earth’s moon forming impact (Canup 2004) falls in between the graze and merge and merging categories. The majority of the impact scenarios summarized above have left a distinct type of observable satellite or family system in the solar system.

The modeled impact scenarios that reproduce the Pluto and Haumea systems are strikingly similar. The impact velocities, impact parameters, and masses of the projectile are almost exactly the same, with the primary difference being the mass ratio between the projectile and target: 0.3 for Pluto (Canup 2005) and 1.0 for Haumea. What is the likelihood of such impact events? The Kuiper Belt is presently composed of multiple dynamically distinct sub-populations (e.g., classical, scattered and resonant, Morbidelli et al. 2008). There is strong evidence for an excitation event after an initial period of collisional growth. The Haumea family must have formed after the excitation event, which would have scattered away all the family members. Although collision probabilities between two 1000-km scale bodies in the classical population are negligible, Levison et al. (2008) calculated up to a  $\sim 50\%$  probability of the impact scenario proposed by Brown et al. (2007) if the two bodies originated from the scattered population and then entered the classical population as a result of the impact. However, the estimated mean impact velocity between scattered objects is substantially higher (about  $2.7 \text{ km s}^{-1}$ ) than we find for the Haumea-forming event. The probabilities of slower speed collisions need to be investigated.

## 5. CONCLUSIONS

In this work, we show that a graze and merge collision event between nearly equal mass bodies is able to produce a symmetrically-elongated, fast-spinning primary, a family of collisional fragments, and multiple bound satellites. The satellites and family members are derived from the icy mantle of the merged, differentiated primary. The family members have a small relative velocity with respect to the primary. This scenario matches all of the observed characteristics of the Haumea system. Our results predict that observations of future family members should all have relative velocities less than  $\sim 0.5V_{\text{esc}}$  of Haumea and that the family members should not be isotropically distributed because they formed in a plane.

We now have the tools to read the record of giant col-

lisions throughout the solar system. At present, there are several 10’s of Pluto-sized bodies known in the outer solar system (Brown 2008). The new Pan-STARRS observatory will detect up to an order of magnitude more bodies in the Kuiper Belt (Trujillo 2008), which will complete the Haumea system and test the predictions of the graze and merge scenario. Models of the dynamical evolution of the Kuiper Belt indicate that the population must have been much larger in the past (by a factor of e.g.  $\sim 1000$ ) (Morbidelli et al. 2008). Satellite formation was a common outcome of giant impacts, and the abundance of satellites around dwarf planets indicates that giant impacts were frequent. We find that the types of collision events that formed the observed satellites and families in the outer solar system are distinctly different from the Earth’s moon formation and families in the asteroid belt. The narrow range of impact parameters that formed the Pluto and Haumea systems place strong constraints on the dynamical history of the largest bodies in the Kuiper Belt.

*Acknowledgements.* We thank D. Ragozzine and M. Čuk for helpful discussions. The hydrocode calculations were run on the Odyssey cluster supported by the Harvard FAS Research Computing Group. The N-body calculations were run using the University of Cambridge, Astrophysical Fluids Research Group computational facilities. ZML is supported by a STFC fellowship; STS by NASA grant # NNX09AP27G.

## REFERENCES

- Asphaug, E., Agnor, C. B., & Williams, Q. 2006, *Nature*, 439, 155
- Asphaug, E., Ostro, S. J., Hudson, R. S., Scheeres, D. J., & Benz, W. 1998, *Nature*, 393, 437
- Barnes, J., & Hut, P. 1986, *Nature*, 324, 446
- Benz, W., Anic, A., Horner, J., & Whitby, J. A. 2007, *Space Science Reviews*, 132, 189
- Benz, W., & Asphaug, E. 1999, *Icarus*, 142, 5
- Benz, W., Slattery, W. L., & Cameron, A. G. W. 1986, *Icarus*, 66, 515
- . 1988, *Icarus*, 74, 516
- Brown, M. E. 2008, in *The Solar System Beyond Neptune*, ed. M. A. Barucci, H. Boehnhardt, D. P. Cruikshank, & A. Morbidelli, 335–344
- Brown, M. E., Barkume, K. M., Ragozzine, D., & Schaller, E. L. 2007, *Nature*, 446, 294
- Brown, M. E., van Dam, M. A., Bouchez, A. H., Le Mignant, D., Campbell, R. D., Chin, J. C. Y., Conrad, A., Hartman, S. K., Johansson, E. M., Lafon, R. E., Rabinowitz, D. L., Stomski, Jr., P. J., Summers, D. M., Trujillo, C. A., & Wizinowich, P. L. 2006, *ApJL*, 639, L43
- Canup, R. M. 2004, *Icarus*, 168, 433
- . 2005, *Science*, 307, 546
- Canup, R. M., Ward, W. R., & Cameron, A. G. W. 2001, *Icarus*, 150, 288
- Collins, G. S., Kenkmann, T., Osinski, G. R., & Wunnemann, K. 2008, *Meteoritics and Planetary Science*, 43, 1955
- Crawford, D. 1999, Adaptive mesh refinement in CTH, Technical report SAND99-1118C, Sandia National Laboratories, Albuquerque, NM
- Durda, D. D., Bottke, W. F., Enke, B. L., Merline, W. J., Asphaug, E., Richardson, D. C., & Leinhardt, Z. M. 2004, *Icarus*, 170, 243
- Gingold, R. A., & Monaghan, J. J. 1977, *MNRAS*, 181, 375
- Holsapple, K. A. 2007, *Icarus*, 187, 500
- Lacerda, P. 2009, *AJ*, 137, 3404
- Lacerda, P., Jewitt, D., & Peixinho, N. 2008, *AJ*, 135, 1749
- Leinhardt, Z. M., & Richardson, D. C. 2002, *Icarus*, 159, 306
- . 2005, *Icarus*, 176, 432
- Leinhardt, Z. M., Richardson, D. C., & Quinn, T. 2000, *Icarus*, 146, 133
- Leinhardt, Z. M., & Stewart, S. T. 2009, *Icarus*, 199, 542
- Leinhardt, Z. M., Stewart, S. T., & Schultz, P. H. 2008, in *The Solar System Beyond Neptune*, ed. M. A. Barucci, H. Boehnhardt, D. P. Cruikshank, & A. Morbidelli, 195–211
- Levison, H. F., Morbidelli, A., Vokrouhlický, D., & Bottke, W. F. 2008, *AJ*, 136, 1079
- Lockwood, A., & Brown, M. E. 2009, in *AAS/Division for Planetary Sciences Meeting Abstracts*, Vol. 41, AAS/Division for Planetary Sciences Meeting Abstracts, 65.06–+
- Lucy, L. B. 1977, *AJ*, 82, 1013
- Maeno, N., Arakawa, M., Yasutome, A., Mizukami, N., & Kanazawa, S. 2003, *Canadian Journal of Physics*, 81, 241
- Marcus, R. A., Stewart, S. T., Sasselov, D., & Hernquist, L. 2009, *ApJL*, 700, L118
- Marinova, M. M., Aharonson, O., & Asphaug, E. 2008, *Nature*, 453, 1216
- McGlaun, J. M., Thompson, S. L., & Elrick, M. G. 1990, *Journal of Impact Engineering*, 10, 351
- McKinnon, W., Prialnik, D., Stern, S., & Coradini, A. 2008, in *The Solar System Beyond Neptune*, ed. M. A. Barucci, H. Boehnhardt, D. P. Cruikshank, & A. Morbidelli, 213–241
- McKinnon, W., Simonelli, D., & Schubert, G. 1997, in *Pluto and Charon*, ed. S. Stern & D. Tholen, 295–343
- Melosh, H. J. 2007, *Meteoritics and Planetary Science*, 42, 2079
- Michel, P., Benz, W., & Richardson, D. C. 2003, *Nature*, 421, 608
- . 2004, *Planet. Space Sci.*, 52, 1109
- Morbidelli, A., Levison, H., & Gomes, R. 2008, in *The Solar System Beyond Neptune*, ed. M. A. Barucci, H. Boehnhardt, D. P. Cruikshank, & A. Morbidelli, 275–292
- Nesvorný, D., Enke, B. L., Bottke, W. F., Durda, D. D., Asphaug, E., & Richardson, D. C. 2006, *Icarus*, 183, 296
- Noll, K., Grundy, W., Chiang, E., Margot, J., & Kern, S. 2008, in *The Solar System Beyond Neptune*, ed. M. A. Barucci, H. Boehnhardt, D. P. Cruikshank, & A. Morbidelli, 345–363
- Pinilla-Alonso, N., Brunetto, R., Licandro, J., Gil-Hutton, R., Roush, T. L., & Strazzulla, G. 2009, *A&A*, 496, 547
- Rabinowitz, D. L., Barkume, K., Brown, M. E., Roe, H., Schwartz, M., Tourtellotte, S., & Trujillo, C. 2006, *ApJ*, 639, 1238
- Rabinowitz, D. L., Schaefer, B. E., Schaefer, M., & Tourtellotte, S. W. 2008, *AJ*, 136, 1502
- Ragozzine, D., & Brown, M. E. 2007, *AJ*, 134, 2160
- . 2009, *AJ*, 137, 4766
- Richardson, D. C., Quinn, T., Stadel, J., & Lake, G. 2000, *Icarus*, 143, 45
- Schaller, E. L., & Brown, M. E. 2007, *ApJL*, 659, L61
- . 2008, *ApJL*, 684, L107
- Schlichting, H., & Sari, R. 2009, *ApJ*, 700, 1242
- Senft, L. E., & Stewart, S. T. 2008, *Meteoritics and Planetary Science*, 43, 1993
- Springel, V. 2005, *MNRAS*, 364, 1105
- Stansberry, J., Grundy, W., Brown, M., Cruikshank, D., Spencer, J., Trilling, D., & Margot, J.-L. 2008, in *The Solar System Beyond Neptune*, ed. M. A. Barucci, H. Boehnhardt, D. P. Cruikshank, & A. Morbidelli, 161–179
- Stewart, S., Seifert, A., & Obst, A. W. 2008, *Geophysical Research Letters*, 35, L23203
- Stewart, S. T., & Leinhardt, Z. M. 2009, *ApJL*, 691, L133
- Trujillo, C. A. 2008, in *The Solar System Beyond Neptune*, ed. M. A. Barucci, H. Boehnhardt, D. P. Cruikshank, & A. Morbidelli, 573–585